1.0

1.1

1.25

4.5
5.0
5.6

2.8

3.2

3.6

4.0

2.5

2.2

2.0

1.8

1.4 1.6

MICROCOPY RESOLUTION TEST CHART
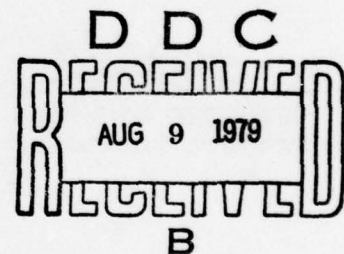NATIONAL BUREAU OF STANDARDS-1963-A

AFML-TR-79-4020

AD A072477

IMPACT INDUCED TENSILE FAILURES IN STEEL

Stephan J. Bless
John P. Barber

University of Dayton Research Institute
300 College Park Avenue
Dayton, Ohio 45469

February 1979

Technical Report
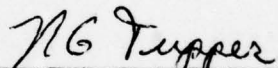
79 08 08 056

NOTICE

When Government drawings, specifications, or other data are used for any purpose other than in connection with a definitely related Government procurement operation, the United States Government thereby incurs no responsibility nor any obligation whatsoever; and the fact that the government may have formulated, furnished, or in any way supplied the said drawings, specifications, or other data, is not to be regarded by implication or otherwise as in any manner licensing the holder or any other person or corporation, or conveying any rights or permission to manufacture, use, or sell any patented invention that may in any way be related thereto.

This report has been reviewed by the Information Office (OI) and is releasable to the National Technical Information Service (NTIS). At NTIS, it will be available to the general public, including foreign nations.

This technical report has been reviewed and is approved for publication.

THEODORE NICHOLAS, AFML/LLN
Project Engineer

NATHAN G. TUPPER, Chief
Metals Behavior Branch
Metals and Ceramics Division

If your address has changed, if you wish to be removed from our mailing list, or if the addressee is no longer employed by your organization please notify AFML, W-PAFB, OH 45433 to help us maintain a current mailing list.

Copies of this report should not be returned unless return is required by security considerations, contractual obligations, or notice on a specific document.

REPORT DOCUMENTATION PAGE	READ INSTRUCTIONS BEFORE COMPLETING FORM

1. REPORT NUMBER	2. GOVT ACCESSION NO.	3. RECIPIENT'S CATALOG NUMBER
AFML-TR-79-4020		

4. TITLE (and Subtitle)	5. TYPE OF REPORT & PERIOD COVERED
IMPACT INDUCED TENSILE FAILURES IN STEEL	Technical Report
	6. PERFORMING ORG. REPORT NUMBER
	UDR-TR-78-56

7. AUTHOR(s)	8. CONTRACT OR GRANT NUMBER(s)
Stephan J. Bless John P. Barber	F33615-76-C-5124

9. PERFORMING ORGANIZATION NAME AND ADDRESS	10. PROGRAM ELEMENT, PROJECT, TASK AREA & WORK UNIT NUMBERS
University of Dayton Research Institute 300 College Park Dayton, Ohio 45469	7E 61102F 2307-P1-02 P1

11. CONTROLLING OFFICE NAME AND ADDRESS	12. REPORT DATE
Air Force Materials Laboratory/LLN Wright-Patterson Air Force Base, OH 45433	February 1979
	13. NUMBER OF PAGES
	44

14. MONITORING AGENCY NAME & ADDRESS(if different from Controlling Office)	15. SECURITY CLASS. (of this report)
55 P	UNCLASSIFIED
	15a. DECLASSIFICATION/DOWNGRADING SCHEDULE

16. DISTRIBUTION STATEMENT (of this Report)

Approved for public release; distribution unlimited

17. DISTRIBUTION STATEMENT (of the abstract entered in Block 20, if different from Report)

DDC
RECEIVED
AUG 9 1979
B

18. SUPPLEMENTARY NOTES

19. KEY WORDS (Continue on reverse side if necessary and identify by block number)

Spall, strain rate, tensile failure

20. ABSTRACT (Continue on reverse side if necessary and identify by block number)

Steel spheres 11 mm in diameter struck hemispherical and cylindrical targets at 3 km/s. Materials were AISI 1020 and 4340. Tensile strength of these materials at strain rates of $10^{-4}s^{-1}$ to 10^3s^{-1} was determined and important rate effects were observed.

Peak particle velocity as a function of range and angle was measured by a fly-off plate technique. Peak stress was calculated from these data.

DD FORM 1473 EDITION OF 1 NOV 65 IS OBSOLETE
1 JAN 73

.0001/s to 1000/s

105 400

20. ABSTRACT (cont'd)

Failure modes were determined from post-impact analysis of targets. Targets less than 6 cm diameter were totally fragmented. 8 cm diameter hemispheres failed in bi-axial tension. 4 cm thick hemispheres failed by planar spall. Large targets did not undergo gross tensile failure.

PREFACE

TABLE OF CONTENTS

LIST OF ILLUSTRATIONS

LIST OF SYMBOLS

K	Measure of spall damage
n	Exponent describing particle velocity decay
N_o	See Table 1
r	Radial coordinate
R_1	See Table 1
T_1	See Table 1
u	Particle velocity
U_{fs}	Free surface velocity
U_p	Shock particle velocity
γ	Exponent in Equation (1)
σ	Spall threshold
$\sigma_1, \sigma_2, \sigma_3$	See Table 1
σ_{go}	See Table 1
σ_{no}	See Table 1
Θ	Departure angle
K	Bulk modulus
μ	Shear modulus

SECTION I

INTRODUCTION

1.1 BACKGROUND

At first it seems paradoxical that impact of a high-velocity projectile can produce regions of intense tensile stress. The initial stress waves generated from an impact are compressive. However, whenever compressive waves encounter free surfaces, they reflect as tensile, or release waves. When release waves generated at different surface elements intersect, the net pressure may drop to extreme tensile values.

Spall is one consequence of impact-induced tensile stresses which is of extreme practical importance. In ballistic attack of armored vehicles, it is often a major kill mechanism. The research described in this report is part of a continuing effort to develop quantitative models for dynamic tensile processes with particular emphasis on spall formation. The materials of interest are structural steels, and the velocities of interest are those characteristic of explosively-launched projectiles, $\sim$3 km/s.

Results from many previous studies of spall can be found in the literature. Several quantative models for spall formation have been developed. However, quantative results for the case of high velocity (> $\sim$1000 m/s) impacts producing two-dimensional stress fields are not available. Most published data and analyses concern one-dimensional stress fields at impact velocities near that required to initiate spall damage ($\sim$ 150 m/s).

Tensile failure in metals is conventionally described by ultimate stress or ultimate strain. This approach is very useful for describing the results of conventional uniaxial-stress tensile tests. However, an accurate account of dynamic tensile failure requires a much more complete description including:

1. the rate dependence of failure criteria,
2. the effect of nonzero values σ_2 and σ_3, and
3. the effect of stress history.

The approach taken in the work reported here was to carefully study a series of two-dimensional impacts in which dynamic tensile failures were

1

expected. The materials studied were 1020 mild steel and annealed 4340 steel. Well-instrumented experiments were carried out to determine how impact-induced peak stresses were attenuated by release waves. Targets were analyzed post-shot to determine extent and nature of tensile failures. Dynamic Hopkinson bar tests were run to obtain the best values for high strain rate constitutive parameters. Finite difference calculations were run, and the numerical results were checked against measured data for stress decay and tensile failure. Lastly, improved failure modes were developed which optimized agreement between numerical and experimental results. This interim report only treats the experimental results. The analytical work will be presented and compared with the data in a subsequent report.

1.2 LITERATURE REVIEW AND DISCUSSION

Quantitative study of spall instructural steels seems to have commenced about 15 years ago. Observations[1,2,3,4,] and analyses[5] soon established the essential features of dynamic tensile failure in these materials.

- Spall takes place only when a certain critical threshold stress is exceeded (in tension). However, the extent of damage is very sensitive to stress duration. An empirical formula used with some success is

$$K = \int (\sigma - \sigma_o)^\lambda \dot{d}t \qquad (1)$$

where K measures spall damage. Complete failure occurs when K exceeds a critical value, K_c. Problems with this approach are that when λ is not 1 or 2, the quantity K is difficult to interpret physically; and that the stress history after initiation of damage is very difficult to calculate. The time dependence of spall has usually been viewed as a consequence of crack growth. At every stress above some critical lower stress, cracks are formed. However, time is required for them to coalesce into a fracture. The higher the tensile stress, the more cracks nucleate, and the shorter the time required for coalescence.

- Spall surfaces in iron may be rough or smooth, depending on, respectively, whether the release wave causing failures passes through the 130 kbar phases transition or not.

2

- Spall in iron and steel is a brittle failure. It takes
  place by nucleation and growth of flat cracks.

More recent work has been looked at spall phenomena with the aid of
finite difference computer codes[6,7,8].

Mescall and Papirno[8] studied spall in 4340 RC15 steel using an
approach similar to that used in the present program. Flat cylinders were
impacted into thick targets, and corresponding finite difference calcula-
tions (HEMP) were carried out. The velocities employed, however, were
< 1000 m/s, which is much lower than used in the present program. A simple
constitutive model was used which could not treat large plastic deforma-
tion or wave propagation through fractured material. Impact orientation
was also poorly known since the projectiles experienced 30 cm of free
flight prior to impact. Data consisted only of post-test physical
measurement on the specimens. Figure 1 shows calculated pressure profiles
at a time when tensile stresses were very high. The spall model of equation
(1) was used, and the authors stated that best agreement was obtained for

$$\sigma_o = 7 \text{ kbar}$$

$$\lambda = 2$$

$$K_c = 337 \text{ kbar}^2 \text{ } \mu s$$

Given the qualitative nature of the data and the approximations in the
material model, it seems probable that these values are not unique and are
only approximate. A value of 2 for λ is very reasonable, since $\sigma^2 t$ is of
the same form as the most widely accepted criteria for detonation of explo-
sives by shock waves [9,10]. This quantity is approximately equal to the
energy per unit area of the stress pulse.

The NAG (nucleation and growth) description of dynamic failure[11]
has a more physical basis. In this model the number of cracks N_c, is given
by the set of equations

$$N_c = N(t) \exp(-R/R_1) \tag{2}$$

$$\dot{N} = \dot{N}_o \exp\left[\frac{\sigma - \sigma_{no}}{\sigma_1}\right] \quad \sigma < \sigma_{no} \tag{3}$$

$$\dot{R} = T_1(\sigma - \sigma_{go})R \quad \sigma < \sigma_{go} \tag{4}$$
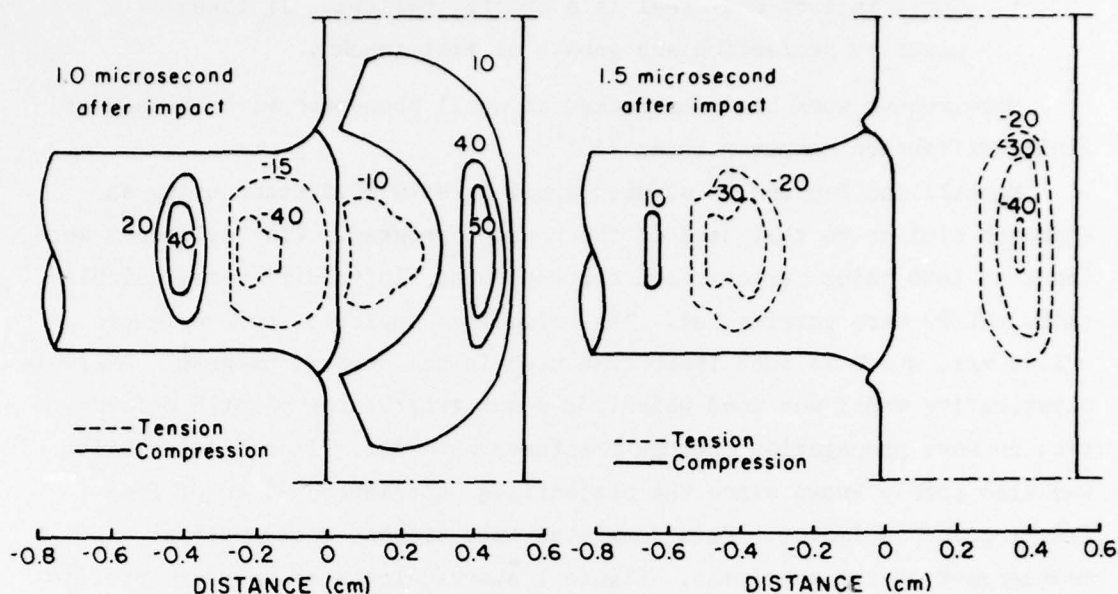
Figure 1. Pressure Contours in kbar 1.0 and 1.5 µs After 762 m/s Impact of Annealed 4340 Projectile onto a Similar Target[8]

Fragmentation can be described by an extension of this model[6] with four additional empirically determined parameters which specify the ratio of the number of fragments to the number of cracks, the ratio of crack radius to fragment radius, the threshold crack volume for fragment formation, and a fragment shape factor.

Values of the parameters in these equations for Armco iron are given in Reference 12, and reproduced herein in Table 1, along with a notation as to their physical significance. The fragmentation parameters were estimated by Reference 7 from parameters for armor steel given in Reference 13. Parameters for a somewhat simplified version of this theory are reported in Reference 6. We see from the table that some spall damage will occur at impact stresses as low as 3 kbar. The NAG equations have apparently only been calibrated for one-dimensional impacts. A typical experimental configuration for a one-dimensional spall experiment is shown in Figure 2. Dynamic spall data are obtained from time-resolved measurements of the free surface velocity, measured at Point A. Figure 3 shows a typical record. The "spall signal" results when the tensile wave, which results when the impact-induced shock reflects at point A, encounters the

4

TABLE 1. FRACTURE AND FRAGMENTATION PARAMETERS FOR
ARMCO IRON FROM REFERENCES 6, 12, AND 13

Parameters	Parameter Definition	Value	Units
T_1	Growth coefficient	-6.0×10^{-4}	$cm^2/dyn/sec$
σ_{go}	Growth threshold	-2.0×10^8	dyn/cm^2
R_1	Nucleation crack size distribution	6.0×10^{-5}	cm
N_o	Nucleation rate coefficient	4.6×10^{12}	$No./cm^3\ sec$
σ_{no}	Nucleation threshold stress	-3.0×10^9	dyn/cm^2
σ_1	Nucleation stress sensitivity	-4.56×10^9	dyn/cm^2
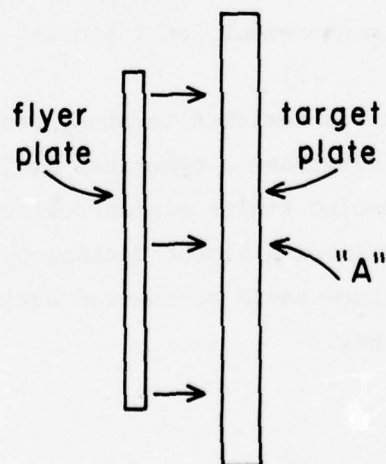
Figure 2. One-dimensional Spall Experiment..

5
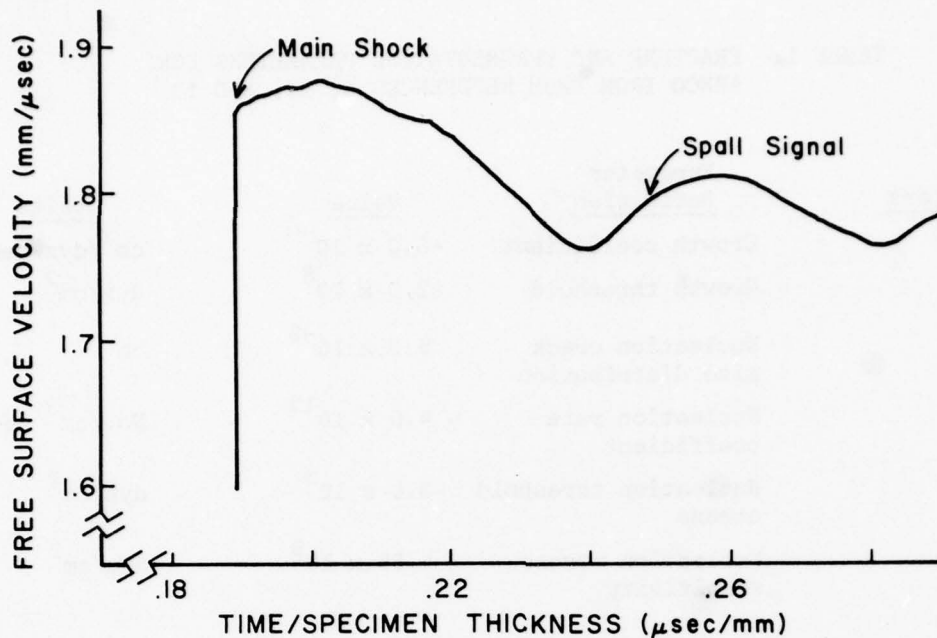
Figure 3. Characteristic Free Surface Velocity Measured at Point A
in Figure 1.2

spalled surface and reflects as a recompression. Reference 7 reports a
sensitivity study for one-dimensional spall in armor iron. N_o was found
to have a major effect on the spall signal. Gross changes in fragmentation
parameters altered the spall signal but not its arrival time. This is
satisfying because N_o and the other crack growth parameters can be
evaluated directly from measurements on the crack populations in shocked
specimens.

The present program was designed to study tensile failure in multi-
dimensional strain configurations. Spherical projectiles were launched at
thick targets. Corresponding finite element calculations were planned by
Major Matuska at the Air Force Armament Technology Laboratory. Calculations
for stress decay and failure could be checked against the data in order to
calibrate the failure model.

6

SECTION II
EXPERIMENTAL PROCEDURE

High velocity impact experiments were used to produce dynamic tensile loads. In this section we describe the experimental approach, hardware, and instrumentation.

2.1 APPROACH

The experiments were carefully designed so that physical processes believed to be important in high velocity ordnance impacts would be activated; however, the geometry was chosen to simplify laboratory procedures and numerical analysis. The principal experimental parameters considered were projectile geometry and material, target geometry and material, and impact velocity.

A spherical projectile geometry was chosen to facilitate both the analytic modeling and the experimental tests. A spherical projectile is axially symmetric, thus permitting adequate modeling with a two-dimensional code. In addition, the spherical projectile, because of its symmetry, does not require control of yaw at impact. Two projectile materials were chosen, SAE-1020 steel and SAE-4340 steel. SAE-1020 steel was chosen as a common, well characterized, mild steel. SAE-4340 steel was chosen as a well-defined standard material which is similar to rolled homogeneous armor (RHA), and which has been previously studied in spall experiments. RHA was not used because of notorious problems with batch-to-batch and through the thickness variations in properties and composition.

Two target geometries were investigated, a right circular cylinder and a hemisphere. These are illustrated in Figure 4. Impact occurred on a flat target surface on the axis of symmetry. The cylinders were intended mainly for technique-development shots. The cylinders were made from 1018 steel, which is essentially identical to 1020 steel. The hemispherical configuration was the basic geometry. This was employed to achieve nearly simultaneous breakout of the impact-induced shock waves at the specimen free surface. Simultaneous shock breakout simplifies the calculation of shock stress from free surface velocity. Variation of shock
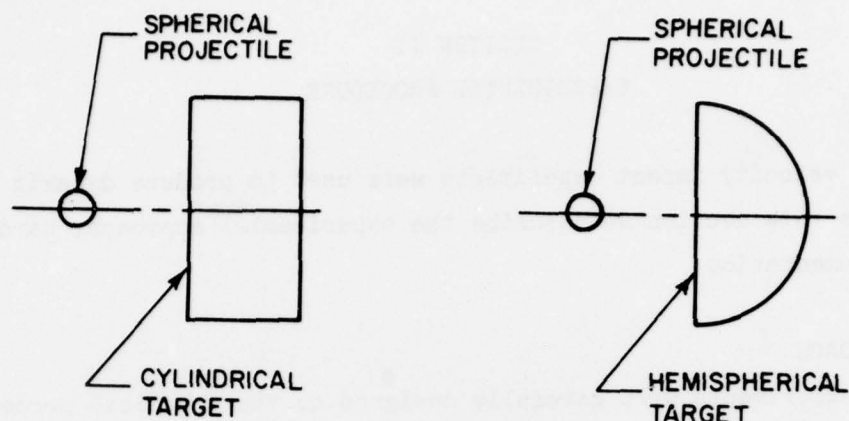
7

Figure 4. Impact Geometries.

properties with direction is also conveniently studied with this geometry.
It was also anticipated that reflection of the shock from the hemispherical
free surface would result in high radial tensile stresses within the target
causing a hemispherical cap to be spalled off the target. The hemispherical
targets were constructed in specific sizes to permit investigation of the
stress field at various radii, r. The radii employed were 2 cm, 3 cm, 4 cm,
6 cm, and 8 cm. These dimensions were chosen based on preliminary analy-
tical results which indicated that target failure and spallation should
occur at approximately r = 4 cm. The thicknesses of the cylinder targets
varied from approximately 2 cm to over 6 cm. The diameter of the cylinder
targets varied from 4 to 8 cm. The same material was used for both the
projectiles and hemispherical targets. The billet materials were subse-
quently characterized as described in Section III.

Impact velocity was in the range expected from conceptual forged
fragment warheads, which weapons achieve velocities in excess of 2 km/s.
Specifically, 3 km/s was chosen as representative. The performance obtain-
able with the two-stage light gas gun employed in this study and described
in Section 2.2 determined the maximum projectile size that could be launched
at this velocity. This was 11.11 mm in diameter, with a mass of 5.6 g.

A summary of the experimental parameters is shown in Table 2.1.

8

TABLE 2.1. EXPERIMENTAL PARAMETERS

Projectile:

        Geometry - Sphere

        Diameter - 11.11 mm

        Material - SAE-1020 and SAE-4340 Steel

Target:

  Cylinder

        Diameter - 4 cm to 8 cm

        Thickness - 2 cm to 6 cm

        Material - SAE-1018 Steel

  Hemisphere

        Diameter - 4 cm to 16 cm

        Material - SAE-1020 and SAE-4340 Steel

2.2 BALLISTIC RANGE DESCRIPTION

A two-stage light gas gun was used to launch the spherical projectiles against the targets. The general layout of the range system is shown in Figure 5. The major components of the range are the light gas gun launch system, the blast tank/sabot separation section, the Hall velocity measurement section, and the target tank area. In addition, Figure 2.2 shows the Dynafax framing camera which was used to observe the target during impact.

The three basic components of the light gas gun are pump tube, in which the gas (usually H_2 or He) is isentropically heated and compressed, a high pressure chamber in which the final stage of compression occurs, and a launch tube in which the projectile is accelerated. The light gas gun used in these experiments consisted of a 40 mm bore 488 cm long pump tube, a 33 cm long high pressure section with a tapered 40 mm chamber, and a 20 mm bore 244 cm long launch tube.

The muzzle end of the launch tube was coupled to a 91 cm diameter, 152 cm long blast tank which was partially evacuated to permit expansion of the hot muzzle gases. Enough air (approximately 0.1 atmospheres) was maintained in the blast tank to cause aerodynamic separation of the sabot
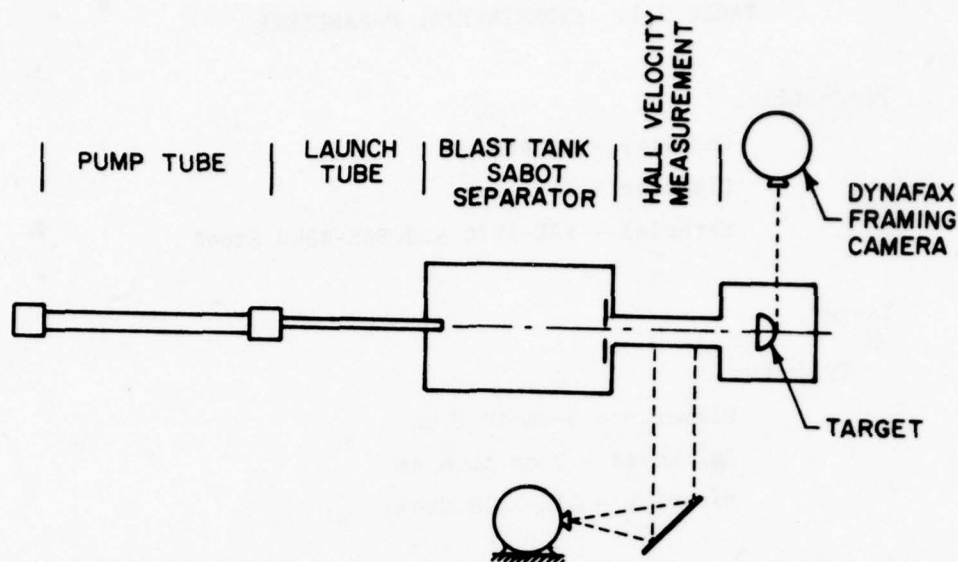
Figure 5. Ballistic Range Configuration

projectile. The exit port of the blast tank was fitted with a sabot
stopper plate which permitted the projectile to fly freely downrange
while intercepting the sabot parts.

Immediately following the blast tank, a Hall velocity measuring
station was located on trajectory. This system used two optical slits
oriented perpendicular to trajectory and 609.6 mm apart. The slits were
illuminated from behind and imaged through mirrors onto the film plane of
a smear camera. The film was traversed in the same direction as the image
of the projectile on the film. As the projectile crossed the slit an image
of the projectile formed on the film. Using the known speed of the film,
the magnification of the system, and the measured position of the image of
the projectile in each slit of the film, the velocity of the projectile was
measured with an accuracy of better than 0.1 percent.

The target tank was attached to the exit side of the Hall velocity
measuring chamber and contained the target with appropriate access for
instrumentation. As shown in Figure 5 the principal target instrumenta-
tion was a Dynafax framing camera. Two ports of the target tank were fitted
with transparent windows to permit backlighting of the target as viewed by
the camera. Target instrumentation will be described in more detail in
Section 2.3.

10

The projectile was launched in a four-piece polycarbonate sabot as illustrated in Figure 6. The sabot was fabricated from polycarbonate stock and designed to support the projectile during launch and to separate freely in the blast tank during free flight.

A velocity loading curve for the gun in this configuration was generated. The powder loads and hydrogen pressure necessary to achieve 3 km/s projectile velocity were determined. The gun was then loaded identically for each shot. The velocities measured during the program varied from 2.89 km/s to 3.34 km/s.

To obtain uniform breakout of the shock on the rear surface of a hemispherical target, the impact had to be very close to the axis of symmetry. Considerable effort went into achieving high impact accuracy. The distance from the gun muzzle to the target was made as small as possible while still permitting adequate sabot separation and accurate velocity measurement. Great care was taken in sabot fabrication and installation to insure clean separation of the sabot from the projectile. The result was that impacts were generally within 1 mm of the aim points. Two data shots were conducted for each configuration to increase the probability of a good on-center impact.
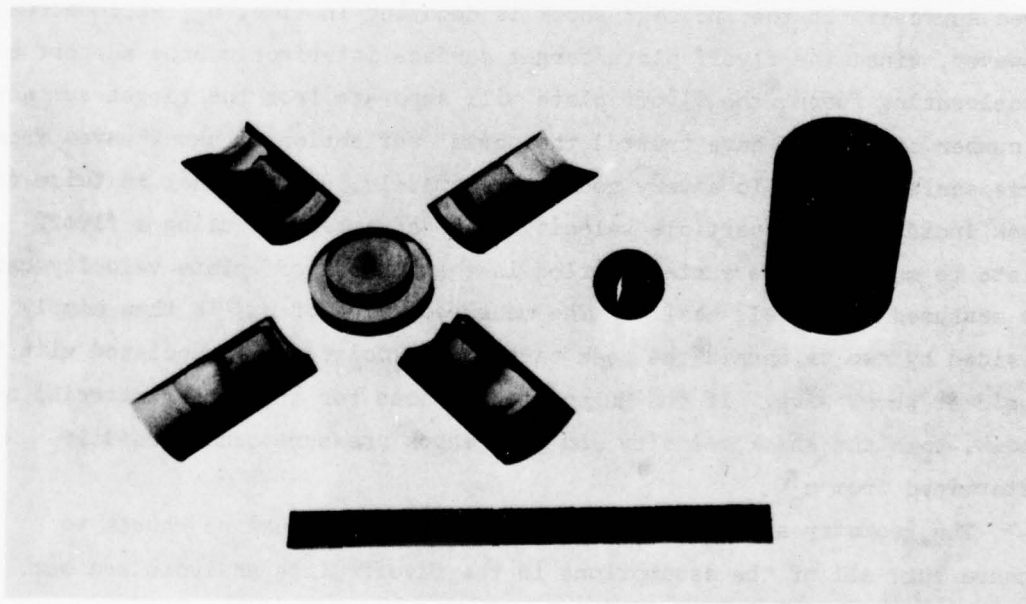

Figure 6. Photograph of the Projectile and Sabot.

11

The entire range, including the blast tank, the Hall velocity measuring station, and the target tank were evacuated to a pressure of approximately 0.1 atmosphere in order to reduce the effect of air shocks on target response and to increase impact accuracy.

2.3 INSTRUMENTATION

One objective of the experiments was to obtain measurements of peak shock stress in the target as a function of radius and departure angle*. Initially, we attempted to measure free surface velocity history with capacitor gauges[14]. Gauges were constructed, calibrated, and placed on the targets. However, due to slight non-simultaneity in shock breakout across the gauge (caused by imprecision in the center of impact), the gauge data could not be quantitatively interpreted.

In order to obtain quantitative data for peak free surface velocity, Hopkinson flyoff plates[15] were successfully employed. Figure 7 illustrates a flyoff plate. It consists of a thin metal disc loosely attached to the target free surface. A shock wave incident on that free surface propagates into the flyoff plate, is reflected from the free surface of the flyoff plate and propagates back into the target. Passage of the shock reflection through the flyoff plate imparts a velocity u_{fs} to the plate and free surface. If the incident shock is decaying in time, u_{fs} will decrease. However, since the flyoff plate/target surface interface cannot support a decelerating force, the flyoff plate will separate from the target surface. A number of authors have treated the normal reflection of shock waves from free surfaces[16]. To a very good approximately, u_{fs} is equal to twice the peak incident shock particle velocity. The advantage of using a flyoff plate to measure free surface motion is that the flyoff plate velocity can be measured relatively easily. The measured value of u_{fs} is then simply divided by two to obtain the peak particle velocity, u_p, associated with the incident shock wave. If the Hugoniot relations for the target material are known, then the shock velocity and peak shock pressure can be readily determined from u_p.

The geometry and material of the flyoff plates must be chosen to insure that all of the assumptions in the flyoff plate analysis are met.

---

*Departure angle is the acute angle between a given direction and the projectile trajectory.

12

INCIDENT
SHOCK
WAVE

V_s

TARGET
SURFACE

FLYOFF
PLATE

t < 0

REFECTED
WAVE

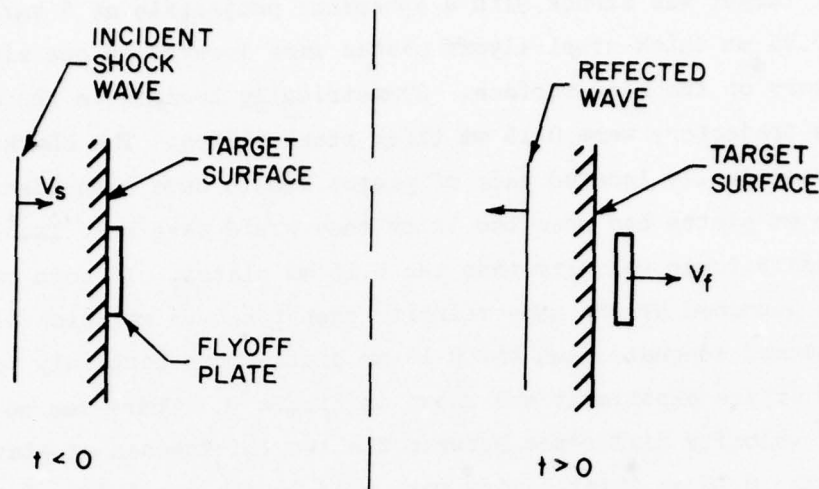TARGET
SURFACE

V_f

t > 0

Figure 7. Flyoff Plate Action

The most important of these assumptions are: (a) the Hugoniot relations for the flyoff plate material are the same as those for the target material; (b) the double transit time through the flyoff plate is less than or equal to the duration of the peak shock pressure; and (c) the effect of shock release from the edges of the flyoff plate is negligible.

Assumption (a) implies, in general, that the flyoff plate must be made of the same material as the target. In this program, flyoff plates were made from steel shim stock. No attempt was made to obtain shim stock of exactly the same alloy as the targets because the Hugoniot relations for steels are relatively independent of steel composition and treatment.

Assumption (b) implies that, in general, flyoff plates must be relatively thin. In order to calculate the required thickness, the duration of the shock at the surface must be known. As this could not be _a priori_ predicted, an experimental determination of required flyoff plate thickness was conducted. The plate velocity is, in effect, a measure of the average particle velocity experienced by the plate during the transit and reflection of the shock[15]; thus, a plate which has a double transit time longer than the duration of the peak shock stress will experience a lower average velocity and will be launched at a velocity less than that associated with

13

the peak shock stress. To address this question, a series of experiments which are illustrated in Figure 8 were conducted. A right circular cylindrical target was struck with a spherical projectile at 3 km/s. A number of 0.25 mm thick steel flyoff plates were located on one side of the trajectory on the rear surface. Symmetrically located on the other side of the trajectory were 0.15 mm thick steel plates. The shock arriving at each symmetrically located pair of plates should have been identical. If the 0.25 mm plates had been too thick they would have been launched at a significantly lower velocity than the 0.15 mm plates. If both sets of plates were launched at the same velocity then the 0.25 mm thick plates could be assumed adequate, and the 0.15 mm plates more certainly adequate. The results of the experiment are shown in Figure 9. There was no significant velocity difference between the two thicknesses of plates. Therefore, the 0.15 mm thick plates were used in the remainder of the study.

Assumption (c) implies that the aspect ratio (diameter to thickness ratio) of the flyoff plates must be large. The diameter of the flyoff plates was arbitrarily chosen to be 6.35 mm. The aspect ratio of the flyoff plates was then approximately 42. Edge effects should provide an insignificant purturbation at this ratio.
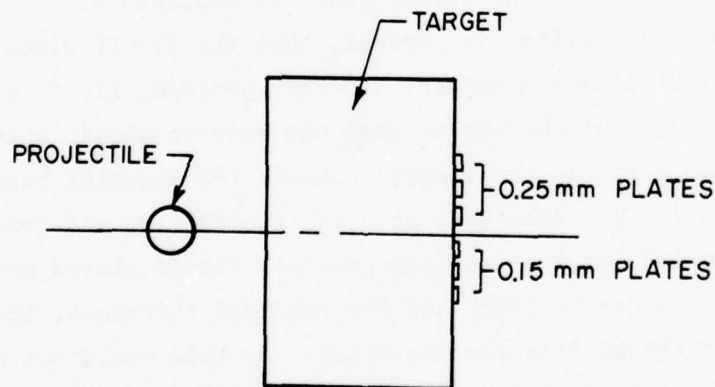

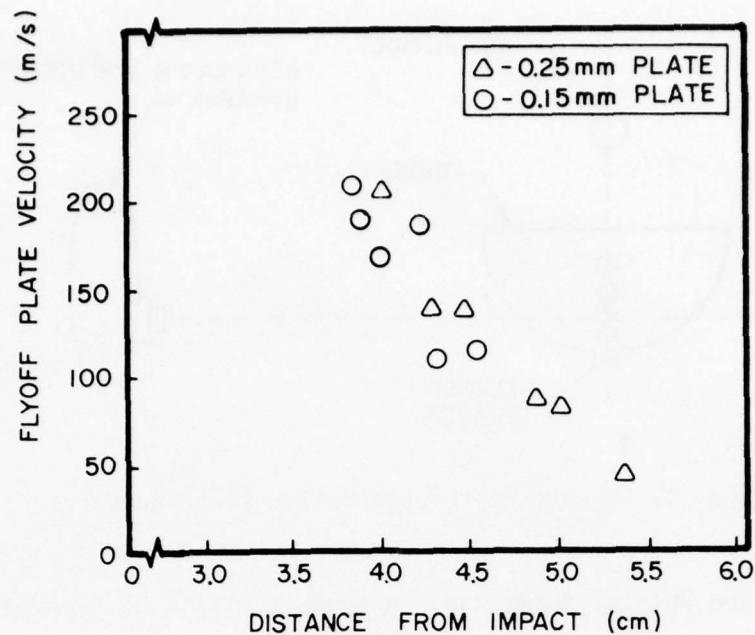Figure 8. Flyoff Plate Thickness Experimental Arrangement

Figure 9.   Comparison of 0.25 mm Thick and 0.15 mm Thick Flyoff Plates

On the hemispherical targets, flyoff plates were located on trajectory and at 10 degree intervals off trajectory up to 80 degrees. The smaller diameter targets (4 cm and 6 cm) posed severe experimental difficulties because they were completely disintegrated by the impact. In addition, because the shock stresses were of relatively long duration, the free surface was launched at nearly the same velocity as the flyoff plates. The presence of debris around the flyoff plates made detection and measurement of their velocities very difficult. Accordingly, on the 4 cm diameter targets, stresses were inferred from free surface velocities using the same analysis as that applied to the flyoff plates. The 6 cm targets proved to be especially difficult. The flyoff plates were very difficult to identify and the free surface velocities gave eratic results. Much of the 6 cm diameter target data was therefore judged to be unreliable.

Flyoff plate motion was recorded using a high speed framing camera. A Beckman and Whitley Dynafax framing at rates of up to 20,000 fps was employed. The camera was arranged to view the back surface of the target in the backlit mode as illustrated in Figure 10. The light source employed
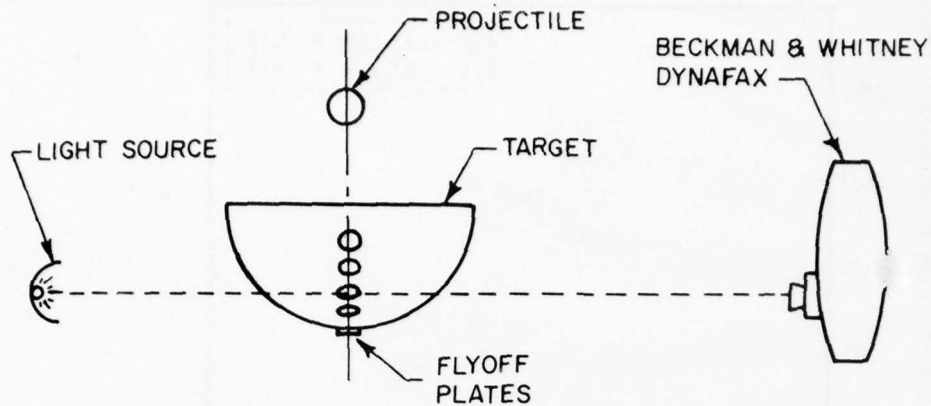
15

Figure 10. Flyoff Plate Observation Technique.

was a Beckman and Whitley Model 358. A typical series of Dynafax frames
showing flyoff plate motion is illustrated in Figure 11. The position
of the flyoff plates was read directly from the film using a traveling
microscope digitizer system. The digitized data were reduced using a digi-
tal computer, and the mean velocity and direction of each plate were
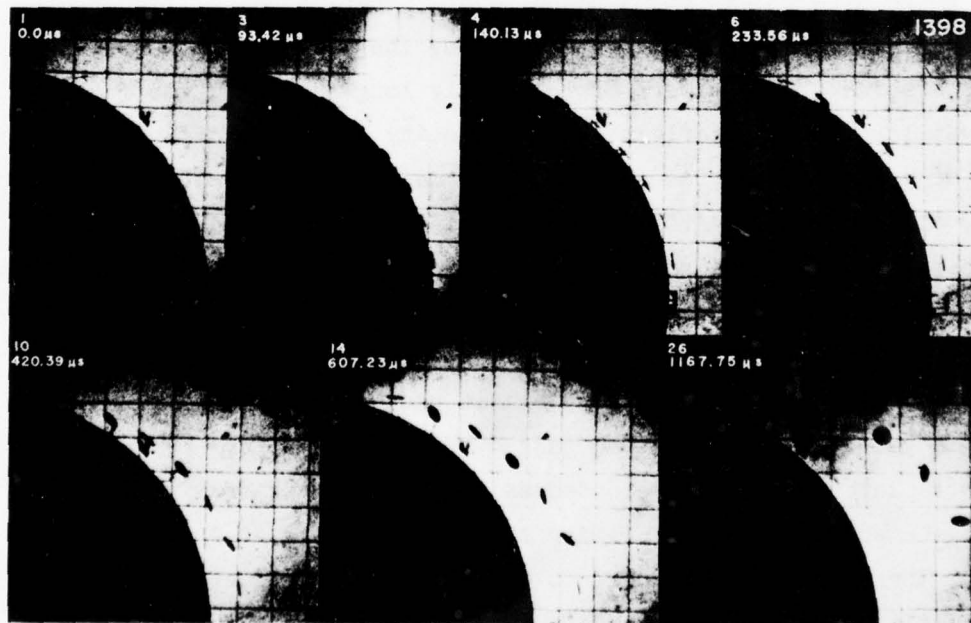calculated. Results are treated in more detail in Section IV.

Figure 11. Flyoff Plate Motion.

16

SECTION III
MATERIAL CHARACTERIZATION

To facilitate the analysis described in Section II , care was made to characterize the materials used in the experiment. Two identical sets of experiments were done, one with SAE-1020 (hot rolled) steel projectiles and targets and the other with annealed SAE-4340 steel projectiles and targets. Certified bars of each material were obtained[*]. All of the projectiles, targets, and test specimens were machined from this material. In addition, a number of specimens were made from each bar to obtain the tensile stress strain properties of the material.

The 4340 was annealed. The hardness of the hemispheres was RC11, the projectiles were RC20, and the tensile specimens were RC10. The 1020 hemispheres were RB44±11. The 1020 projectiles were RB81±2. The tensile specimens were RB67±1.

Tensile properties of these materials were determined at strain rates ranging from $\sim 10^{-4}$/s to ~ 1000/s. Data at strain rates of 10^{-4}/s and 1/s were obtained with a conventional hydraulic materials testing machine. The tension tests at very high strain rates (up to 1000/s) were performed on a split Hopkinson bar apparatus developed at the Air Force Materials Laboratory and described in Reference 17. A small "dog bone" specimen illustrated in Figure 12 was used in all of the tests. The split Hopkinson bar apparatus is capable of testing materials in tension at rates above 10^3/s using a small threaded specimen of 0.318 cm diameter and approximately 2.92 cm length. Data are obtained in the form of load crosshead displacement and cross head displacement rate. Strain is calculated from an empirical formula relating head displacement to strain and gauge length obtained using strain gauges on dummy calibration specimens. The calculated strain is assumed uniform along the gauge length and thus does not take into account necking when it occurs. Strain rate is taken as the time derivative of the "uniform" strain. Strain and strain rate are given in terms of

---

[*]The 4340 was certified by E. M. Jurgensen, Los Angeles the 1020 was cer-
tified by Miami-Dickerson Steel Company, Dayton, Ohio.
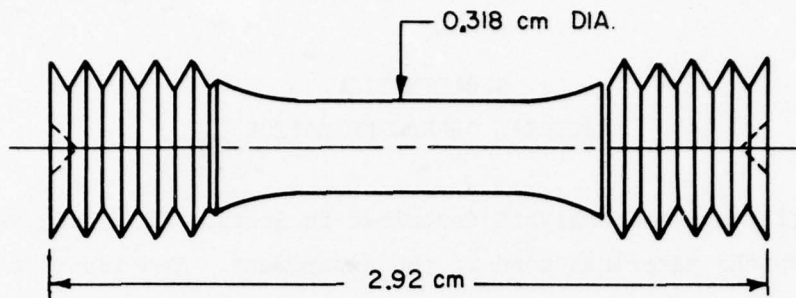
17

Figure 12. Tension on Hopkinson Bar Specimen

engineering strain (δ_1/l_0). True stress is calculated from load divided by actual area (original area corrected to uniform axial strain assuming incompressible plastic flow).

Stress-strain data for SAE-1020 steel and SAE-4340 steel are shown in Figures 13 and 14 respectively. The 1020 data show several strain rate effects. The "overshoot" associated with the upper and lower yield point became much more pronounced in this material at higher strain rates. The yield strength associated with the recovery from the overshoot increased from 329 MPa (3.29 kbar) at 10^{-4}/s to 410 MPa (4.1 kbar) at 1/s, to 660 MPa (6.6 kbar) at 10^3/s. (The nominal value of the yield strength for this material given in handbooks is 400 MPa (4 kbar). There is also no downward turning of the stress strain curve at the highest strain rate; this is apparently associated with the relative decrease in necking with strain rate. At 10^3/s the sample could not be driven to rupture because the load duration was limited to 300 μs.

The effect of strain rate on yielding was also very significant in the 4340 specimens. The proportional limit could not be resolved; however, the yield point associated with the sharp knee in the stress strain curve was 820 MPa (8.2 kbar) at 10^{-4}/s^{-1}, about 830 MPa (8.3 kbar) at 1/s^{-1} and 1130 MPa (11.3 kbar) at 10^3s^{-1}. This is good agreement with the 8.3 kbar value for tensile yield given in Reference 18 for annealed material.
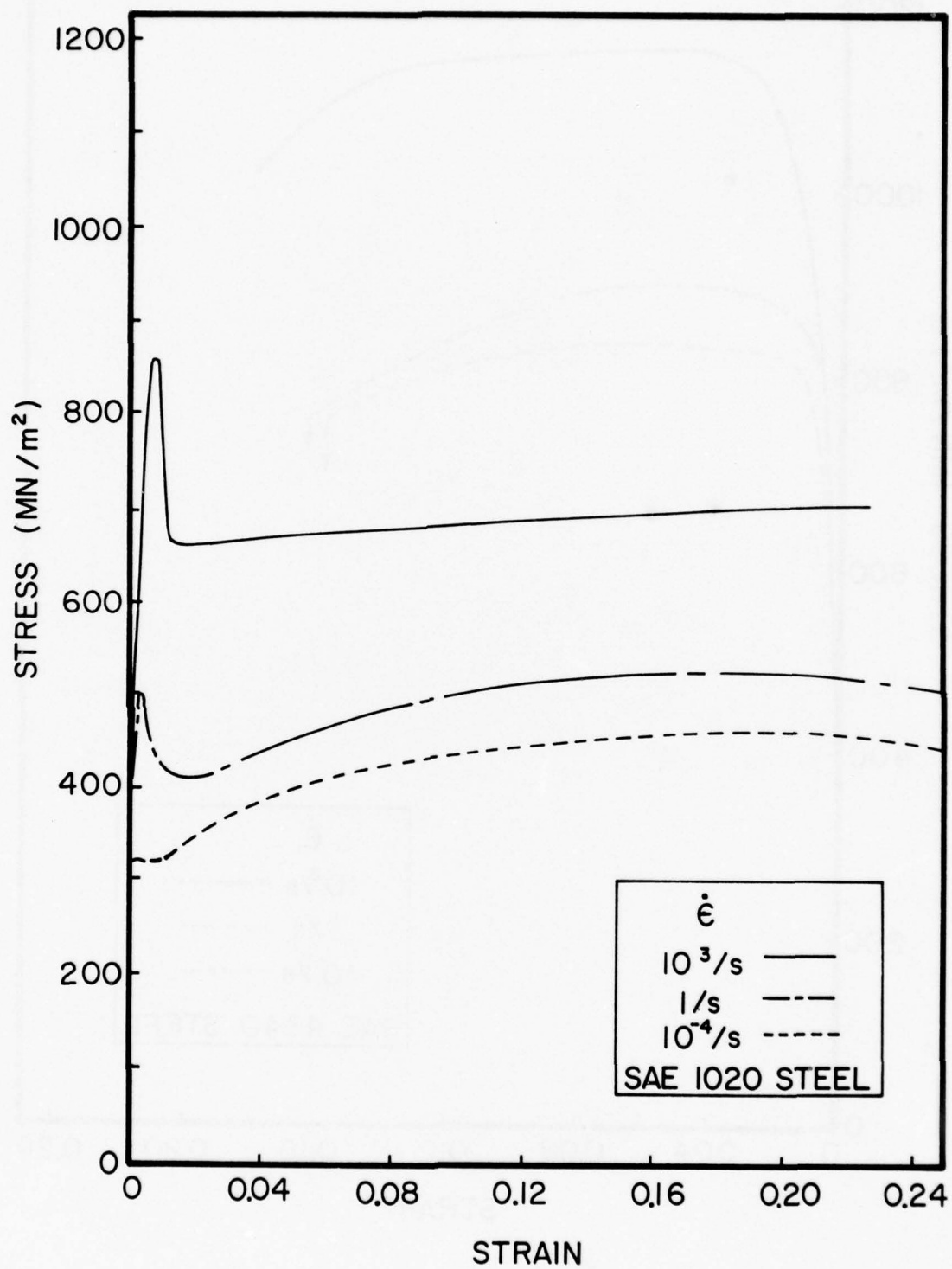
18

Figure 13. Tensile Stress Strain for SAE-1020 Steel
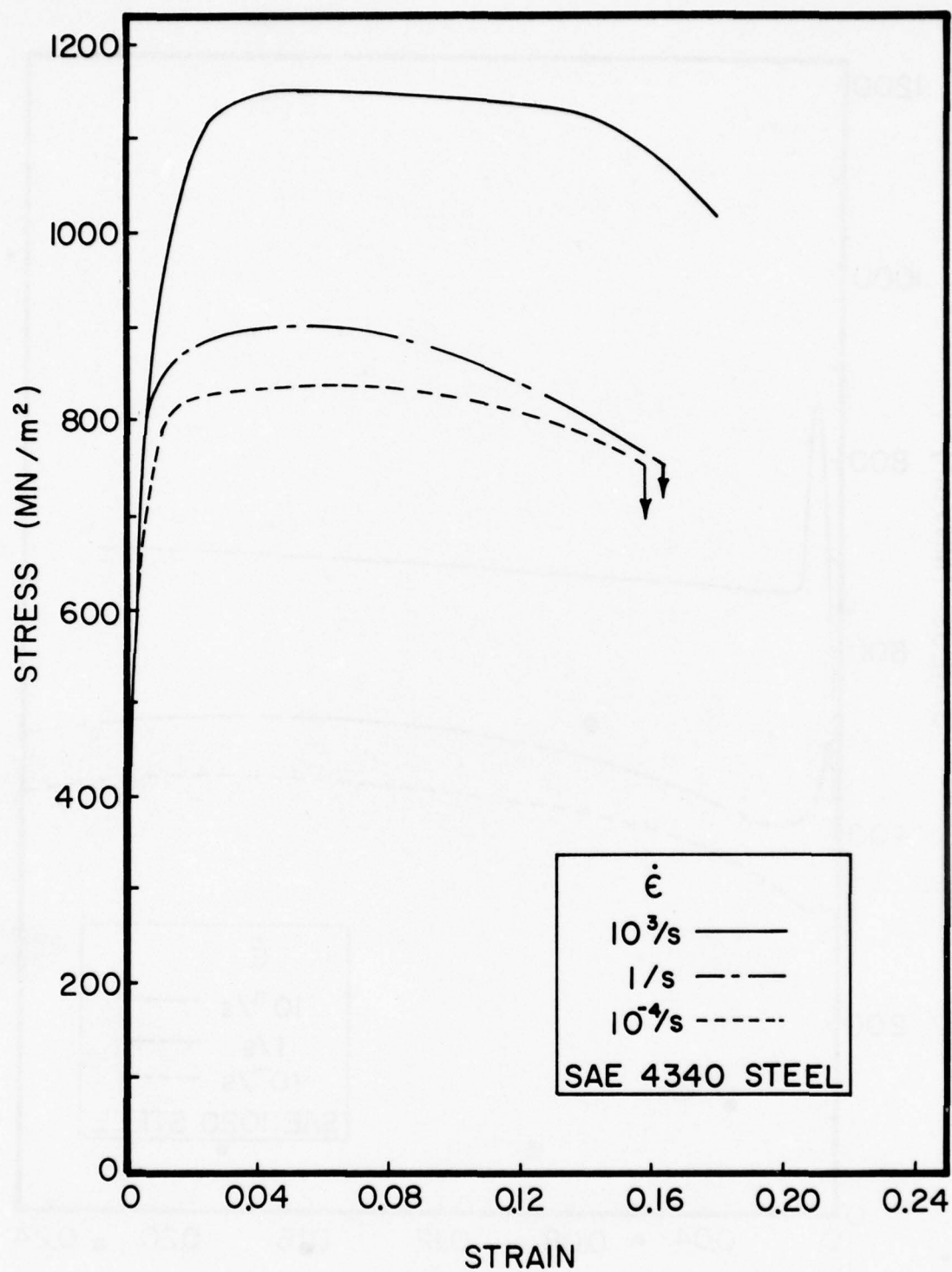$(100 \text{ MN/m}^2 = 1 \text{ kbar})$

19

Figure 14. Tensile Stress Strain for SAE-4340 Steel.
(100 MN/m² = 1 kbar)

20

The ultimate strain at low strain rate was 16 percent. The ultimate strain at high strain rate was not determined due to the loading pulse length limitation.

The data shown in Figures 13 and 14 are in general agreement with previous investigations of strain rate effects in these materials. Reference 19 reviewed five previous investigations of rate effects on tensile yield of mild steel. It was reported that the yield strength increased by about 200 MPa (2 kbar) between $1s^{-1}$ and $5 \times 10^2 s^{-1}$. Butcher and Canon[20] reported significant strain-rate effects in the compressive yield strength of annealed 4340. At static rates, the yield stress (in uniaxial stress) was 5.24 kbar. However, yield under shock compression (uniaxial strain) was at 11.4 kbar. The shock strain rate was about $10^5 s^{-1}$.

Values for the elastic constants for these materials can be taken from the literature[20,21], namely K = 165.7 GPa (1657 kbar) and μ = 81.3 GPa (813 kbar).

SECTION IV
EXPERIMENTAL RESULTS

Experiments were done on SAE-1020 steel hemispheres, SAE-4340 steel hemispheres, and SAE-1018 steel cylinders. In these experiments peak shock stress was measured at the rear free surface of the targets, the failure modes of the target were identified, and a metallographic analysis of the post-impact target was undertaken. In this section we describe the results that were obtained from these experiments.

4.1 SAE-1020 STEEL

Hemispheres with radii (r) of 2 cm, 3 cm, 4 cm, 6 cm, and 8 cm were struck with 11.11 mm diameter steel spheres at 3 km/s. Flyoff plates were attached to the rear surface of each hemisphere; they were placed on-trajectory and at departure angles of 10 degree intervals out to 80 degrees. Peak particle velocity associated with the incident shock wave was determined from the flyoff plate velocity, as explained in Section II. The results for each value of departure angle are displayed in Figures 15 through 23. Each impact configuration was repeated once to obtain redundant data. All the data are displayed in the figures with the exception of some data at r = 3 cm. As explained in Section II, the motion of the flyoff plates on these targets was very difficult to determine, and some data were judged to be uncertain and were omitted from further consideration. The measurements at r = 2 cm were made from the leading edge of the disintegrating target debris.

These figures also include data from the 1018 steel cylinders. The difference in properties between 1020 and 1018 steel were considered insignificant for present purposes. In analyzing the flyoff plate data from the cylindrical targets, it was assumed that the normal component of the flyoff plate velocity was twice the normal component of the incident peak particle velocity. The magnitude of the peak shock particle velocity could then be easily calculated since the particle velocity vector was radial from the impact point.
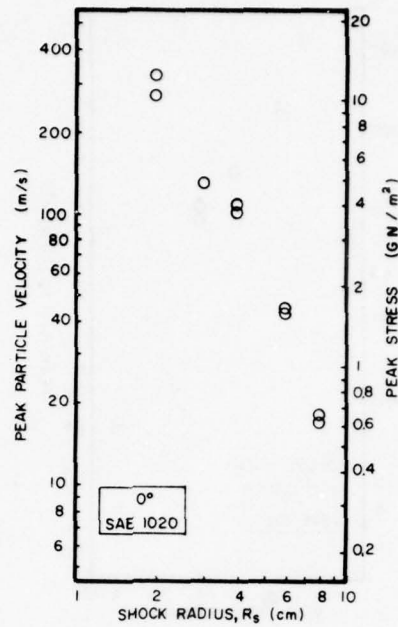
22

Figure 15. Peak Particle Velocity Versus Radius for SAE-1020 Steel at 0°. (1 GN/m² = 10 kbar)
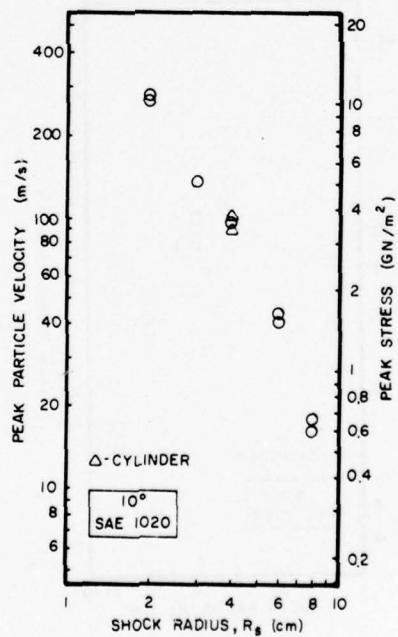

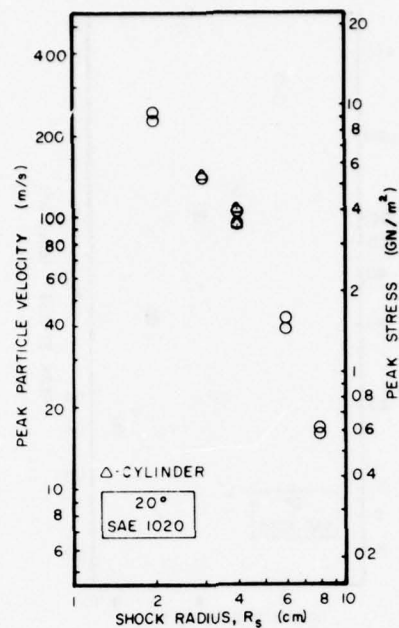Figure 16. Peak Particle Velocity Versus Radius for SAE-1020 Steel at 10°

Figure 17.   Peak Particle Velocity Versus Radius for SAE-1020 Steel at 20°
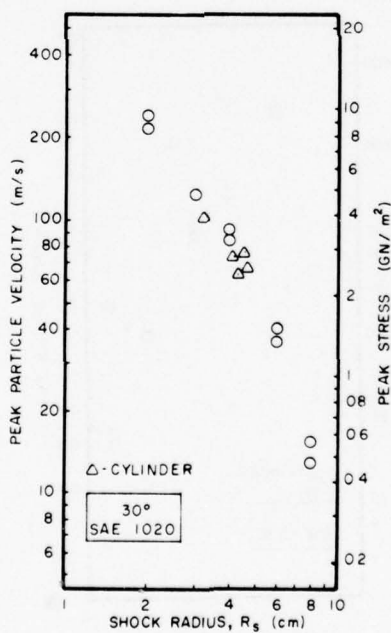

Figure 18.   Peak Particle Velocity Versus Radius for SAE-1020 Steel at 30°
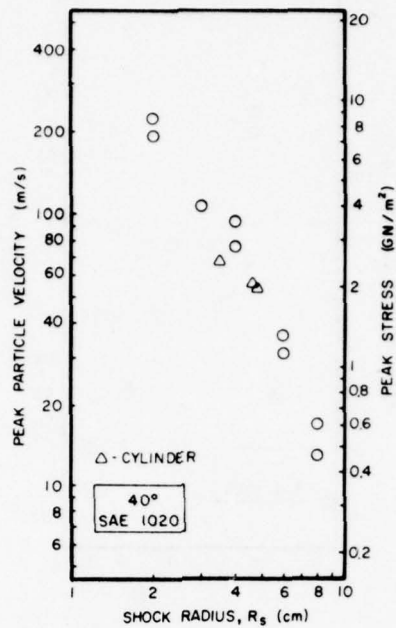
24

Figure 19.   Peak Particle Velocity Versus Radius for SAE-1020 Steel at 40°
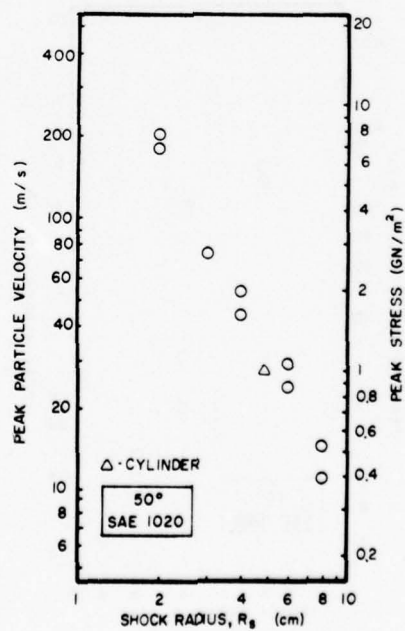

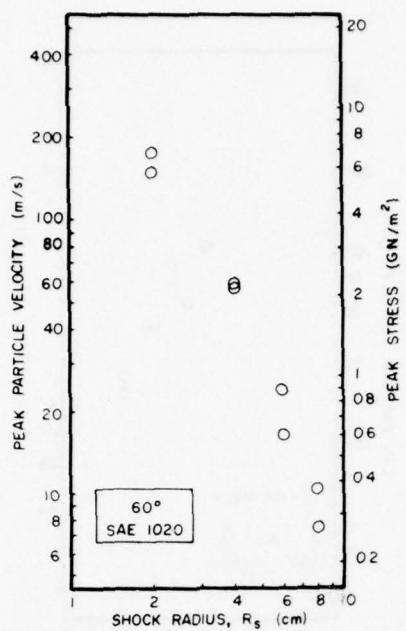Figure 20.   Peak Particle Velocity Versus Radius for SAE-1020 Steel at 50°

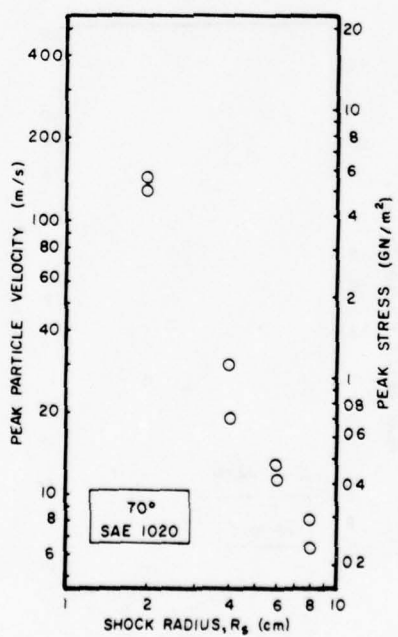Figure 21.   Peak Particle Velocity Versus Radius for SAE-1020 Steel at 60°

Figure 22.   Peak Particle Velocity Versus Radius for SAE-1020 Steel at 70°
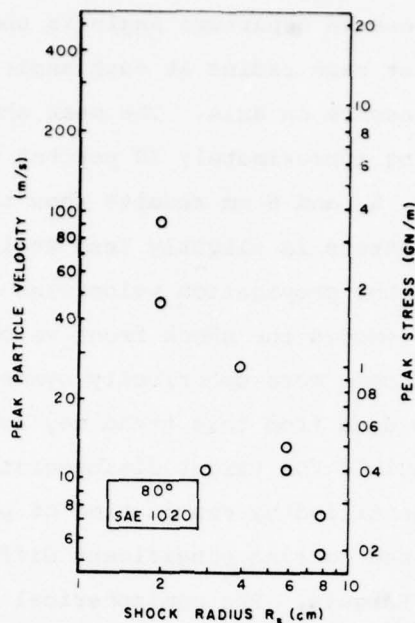
Figure 23.   Peak Particle Velocity Versus Radius for SAE-1020 Steel at 80°

The peak shock stress is also shown in Figures 15 through 23. It was calculated from the peak particle velocity using the low pressure Hugoniot of iron[20]. The stresses vary from around 3 GPa (30 kbar) at r = 2 cm down to 600 MPa (6 kbar) at r = 8 cm. The stress decays with distance nearly as $1/r^2$.

The decay of peak particle velocity with rahge, $\partial \ell n v / \partial \ell n r$, is bilinear for $\Theta \leq 60°$. In otherwords, peak particle velocity varies with range as r^{-n}, and n starts out small and transitions to a larger value at some critical radius. For $0 < \Theta < 30$, the critical radius was at about r = 5.5 cm. For 40° and 50° it was closer to 6 cm, but for 60° it was at r $\sim$ 4 cm. The average and standard deviation for $\partial \ell n u / \partial \ell n r$ for r   5.5 cm was 1.53 and 0.17; the corresponding final values were 2.95 and 0.36, respectively. No change in n could be resolved for $\Theta \geq 70°$; for $\Theta = 70°$, n   2.15. The change in decay rate is probably associated with the overtaking of the initial shock by release waves originating from either the rear surface of the projectile on the front surface of the target. Future finite difference calculations will clarify this point.

27

The dependence of stress on departure angle is shown in Figure 24. In that figure the data for each radius at each angle were averaged and normalized by the peak pressure on axis. The peak shock stress decreased with departure angle, being approximately 30 percent of the on-axis value at 80 degrees. The r = 4, 6, and 8 cm results show that the departure angle dependence of peak stress is slightly less at larger radii. This is an expected result; since the propagation velocities of elastic waves in the shock-compressed material exceed the shock front velocity, the properties of the shock front will become more spherically symmetric with time. The deviation of the r = 2 cm data from this trend may be caused by the physical processes responsible for target disintegration.

Failure modes were identified by examination of post-shot target cross sections. We were surprised to find singificant difference between hemispherical and cylindrical targets. The hemispherical targets did not spall off a cap of material as expected. Instead, failure planes were mainly radial. In the 4 cm diameter targets, fragmentation was complete. The 6 cm diameter targets only fractured in the region along the path of the projectile (Figure 25). Most of the fracture surfaces were very finely textured indicating rapid bulk tensile failure. The rupture surfaces were mainly radial indicating that the principal tensile stress was the hoop component. Within about 1 mm of the free surface the rupture surfaces were smooth and inclined at about 45 degrees to the free surface. This indicates that a thin shell area near the rear surface failed in shear.

Rupture in the 8 cm diameter targets was incipient (Figure 26). Radial cracks formed. Many small cracks were only a few grains long, and there was only a slight tendency for these to be radially aligned. Cracks seemed to form just in a region between 3 and 9 mm from the free surface at departure angles of 0 and ± ∿ 15 degrees. In one of the specimens, a long crack extending from the crater to the free surface occurred (Figure 27). The larger diameter targets did not have any internal rupture surfaces. Figure 28 shows the microstructure of one of the 1020 hemispherical targets in a region where cracks formed but did not coalesce. The orientation of these cracks was almost random with a slight preference for the radial direction. The cross-section in the photomicrograph is a meridian plane. The voids were several times wider
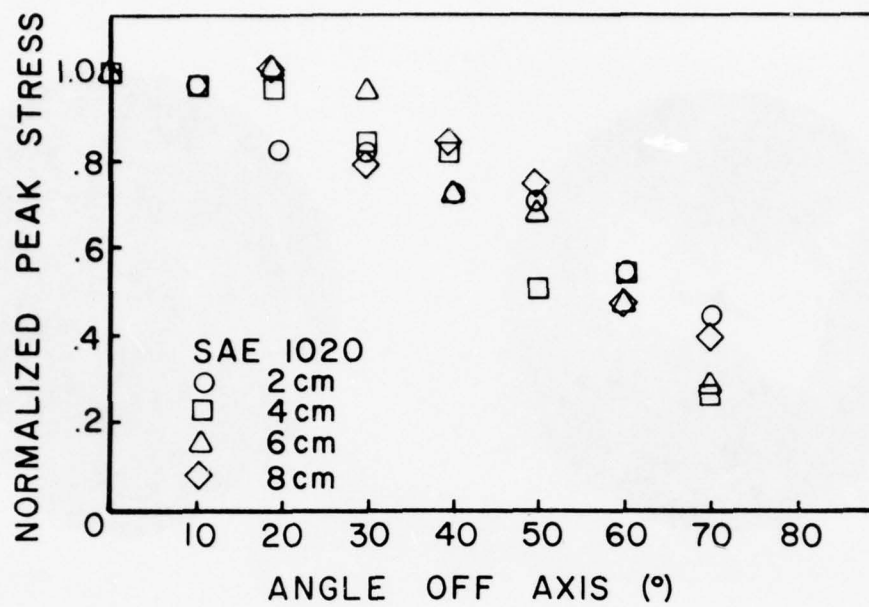
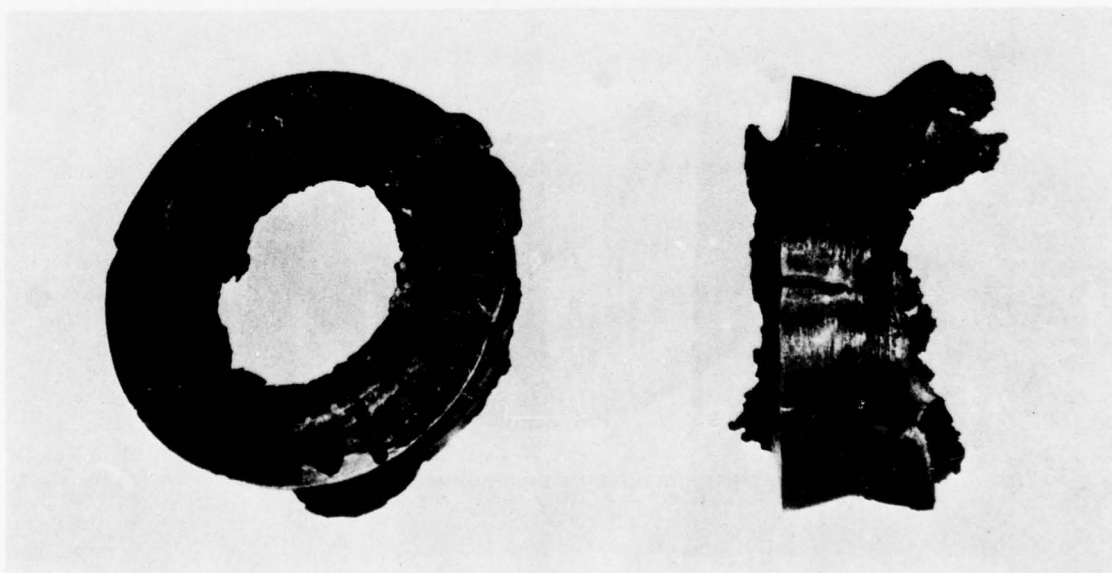Figure 24. Variation of Shock Stress With Angle

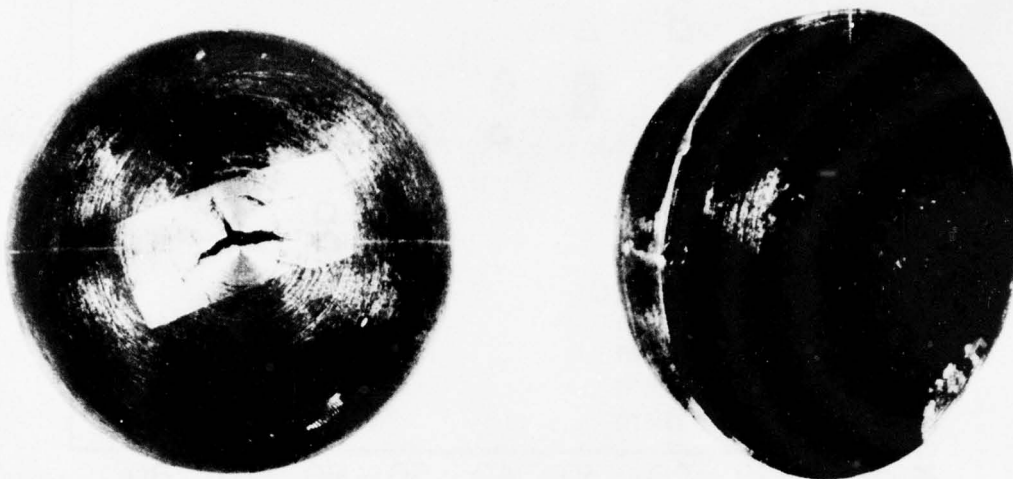Figure 25. Post-impact Condition of a 6 cm Diameter Hemispherical Target

29

Figure 26.   Post-impact Cross-condition of a 8 cm Diameter Target
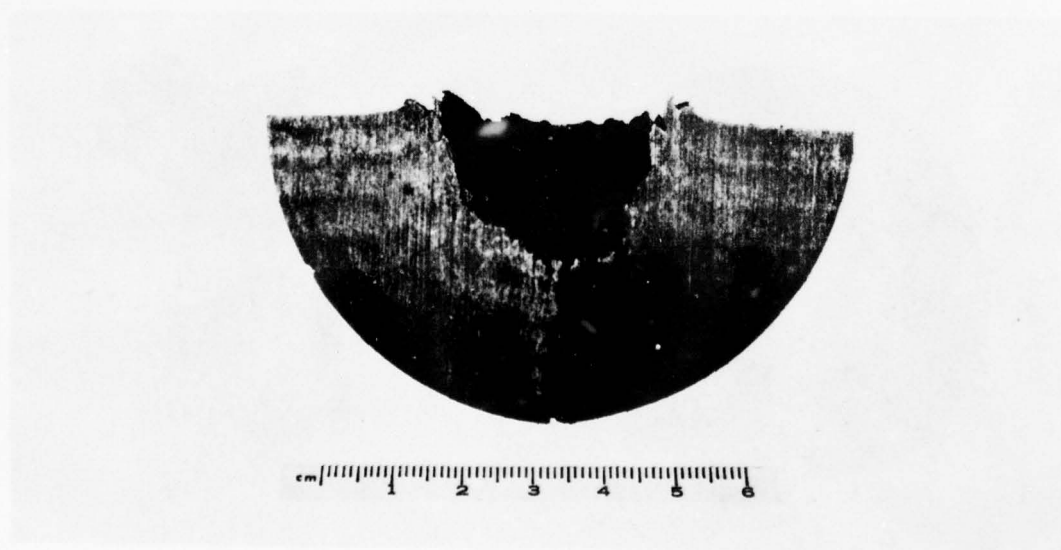

Figure 27.   Post-impact Cross-section of a 8 cm Diameter Target

30

Figure 28. Two Views of the Microstructure of an 8 cm Diameter Target in
a Region of Incipient Failure Near the Free Surface. Note the
Shock-induced Twinning.

than they were deep. In the observation planes the smallest void shapes
were "penny like", but subsequent growth appeared to be in only one
direction. The voids seemed to nucleate in the ferrite. The cracks ran
through pearlite with difficulty, and also ran through adjacent ferrite
grains.

We attempted to locate the $\alpha \overset{\leftarrow}{\to} \epsilon$ phase transition boundary at 13 MPa
(130 kbar) by counting the twin density[23]. However, no sharp discontin-
uities in twin appearance were recognized. This may be due to the fact
that the most highly twinned region also underwent severe plastic deformation
which obscured the twin density. Microhardness traverses were made across
one of the 8 cm diameter 1020 targets. Smith[23] observed a sudden 60 per-
cent increase in VHN at the phase transition boundary. Our results are
shown in Figure 29. The increased hardness near the impact zone is
probably due to the plastic flow which has occurred there. The 13 MPA
(130 kbar) isobar presumably occurred within this region, e.g. at
$r \leq \sim 1.5$ cm. This is consistent with the pressure profile deduced from
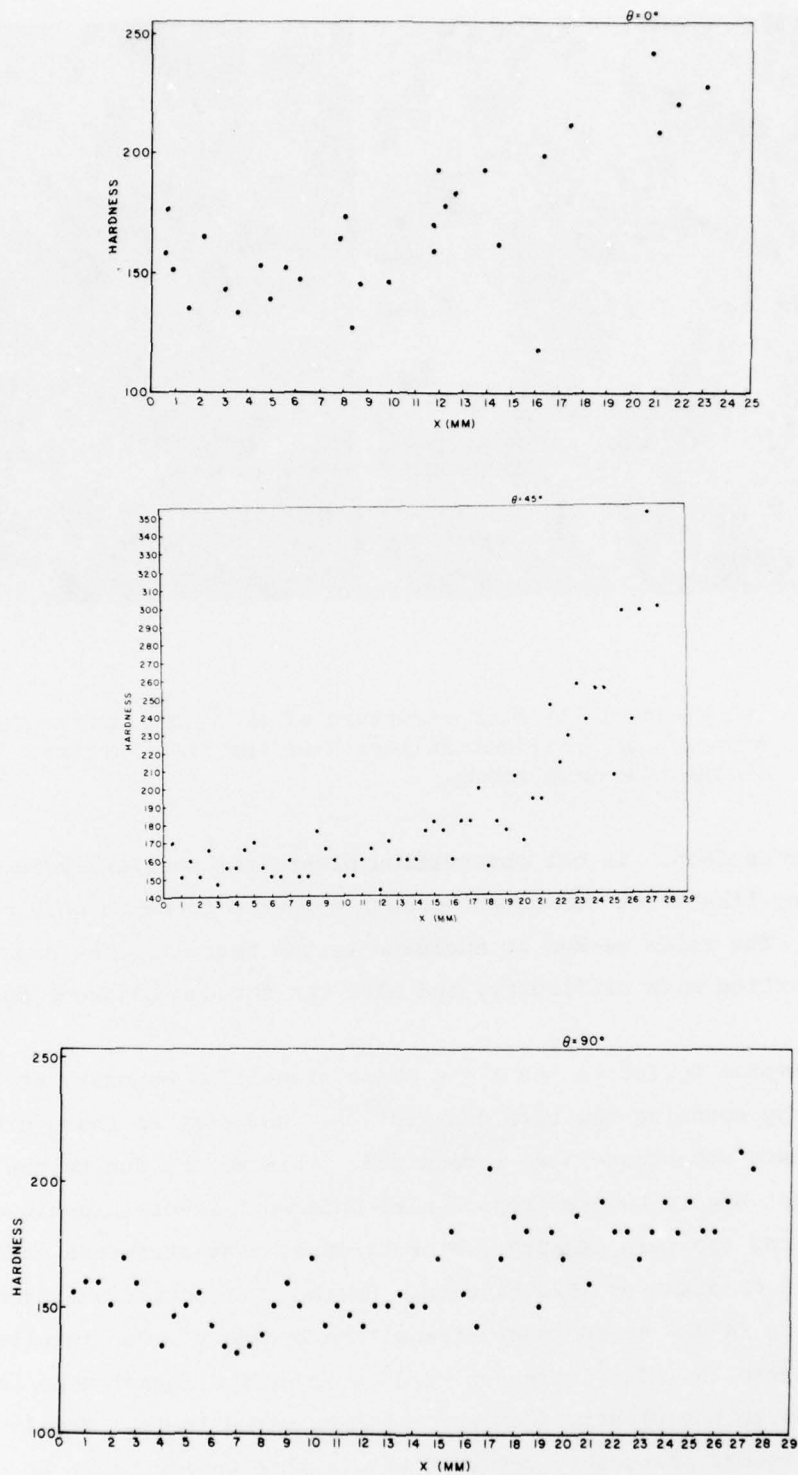the flyoff plate data.

31

Figure 29. Microhardness Measurements on 1020 8 cm Diameter Targets
x = 0 Denotes Spherical Free Surface. (Hardness is VHN
With 100g Load.)

32

The failure mode of the SAE-1018 cylinders was quite different from that displayed by the hemispheres. Failure occurred in the 3 and 4 cm thick specimens. Details of the failure are not reproducible. Of the 3 cm thick targets, one disintegrated and one merely bulged. The failure in the 4 cm thick targets was nearly a planar spall, parallel to the free surface, about 4 mm thick. Pieces are shown in Figure 30. The surface was finely textured and very rough. This is typical of spall in iron which has not experienced a phase transition[1]. There were many "scabs" of up to 1.5 mm thickness. This indicates that the bulk tensile failure occurred over a fairly thick disc-shaped volume.

The differences in failure modes between the cylinders and hemispheres may be explained as follows. The tensile states in the cylinders and hemispheres may be qualitatively described by the sketches in Figure 31. The stress states in both materials are similar during passage of the initial compressive wave, as shown in (a) and (c). In (b) the release wave reflects from the free surface of the hemisphere. The increment in particle velocity behind the release wave is $\frac{1}{2} u_{fs}$, and it is directed radially. The hoop stress increases behind this wave because it accelerates neighboring particles radially, and hoop strain is proportional to radial displacement. The rarefaction wave produced in the cylinder is quite different, as shown in (d). The shock reflection produces a fast distensional release wave and a slower shear wave. Since particle velocity is normal to the release wave front, the vector particle velocity increment behind the wave has a component directed towards the target axis. Thus, passage of this wave results in a total particle velocity which is not purely radial, and which produces less hoop strain than would occur in a hemisphere. Reduction of hoop strain allows strain to develop normal to the free surface which eventually results in spall.

4.2   4340 RESULTS

Annealed 4340 hemispheres of 2, 3, 4, 6, and 8 cm radius were struck with 11.11 mm in diameter spheres at 3 km/s. Flyoff plates were positioned on the rear surface of each hemisphere at 10 degree intervals in the same manner as that employed on the SAE 1020 steel hemispheres reported in subsection 4.1. The results at each angular position on the targets are displayed in Figures 32 through 40. Only one of the impacts at 6 cm

33

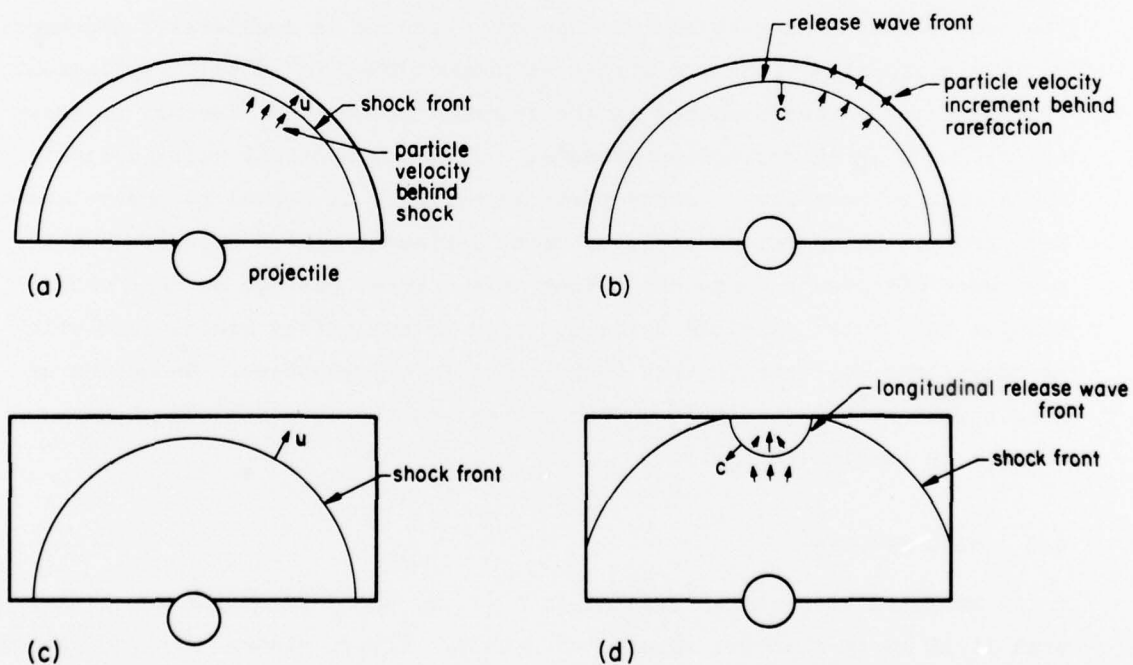Figure 30. Post-impact Condition of a 4 cm Thick Cylinder

Figure 31. Sketches Showing Wave Propagation in Hemispheres and Cylinders. Compressive Wave Propagates at Velocity U and Release Wave With Velocity C. More Hoop Strain Results in Hemispherical Target.
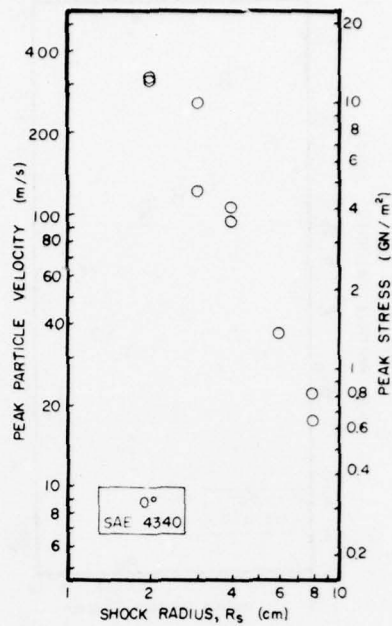
34

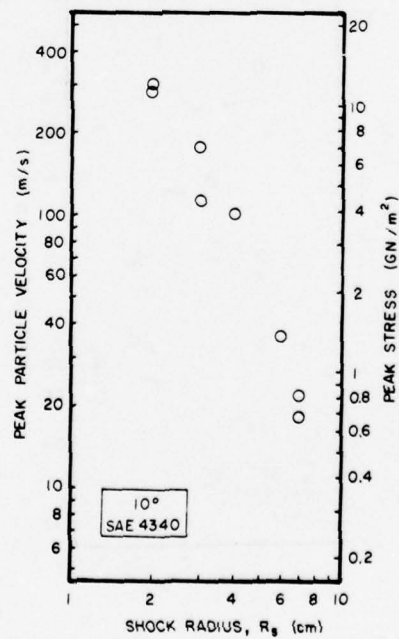Figure 32. Peak Particle Velocity Versus Radius for SAE-4340 Steel at 0°

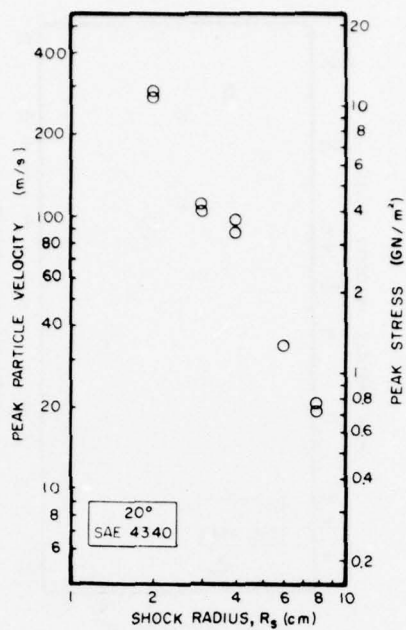Figure 33. Peak Particle Velocity Versus Radius for SAE-4340 Steel at 10°

35

Figure 34. Peak Particle Velocity Versus Radius for SAE-4340 Steel at 20°
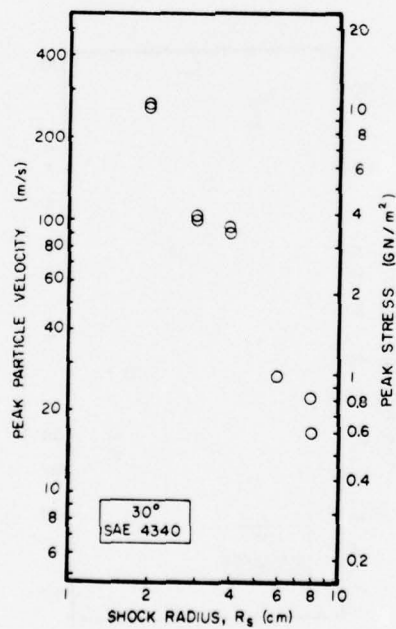

Figure 35. Peak Particle Velocity Versus Radius for SAE-4340 Steel at 30°
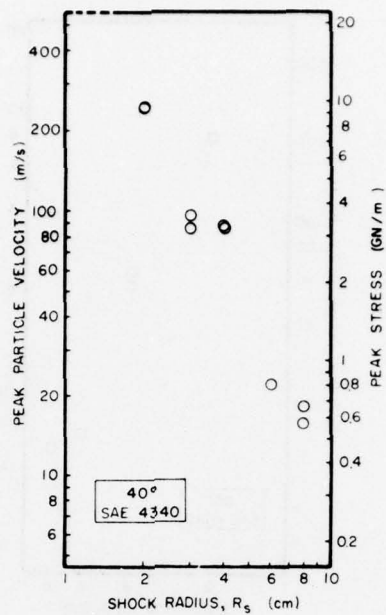
36

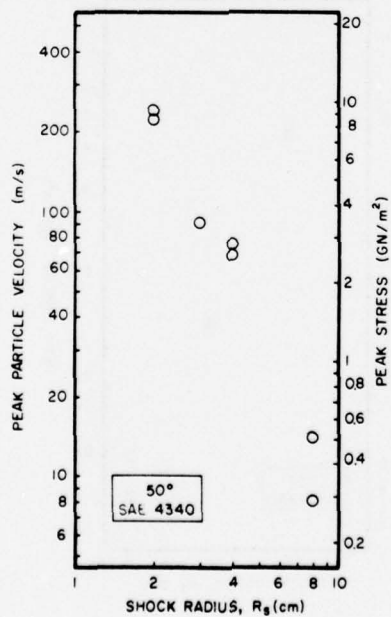Figure 36. Peak Particle Velocity Versus Radius for SAE-4340 Steel at 40°

Figure 37. Peak Particle Velocity Versus Radius for SAE-4340 Steel at 50°
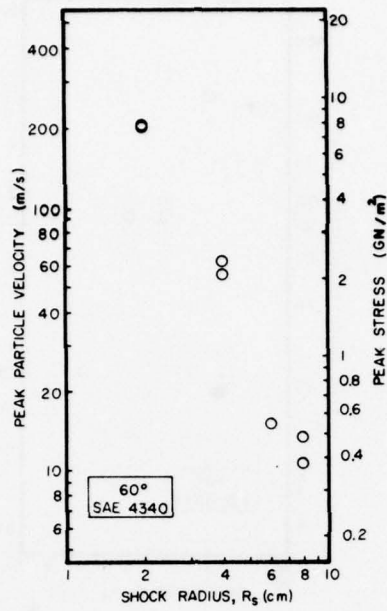
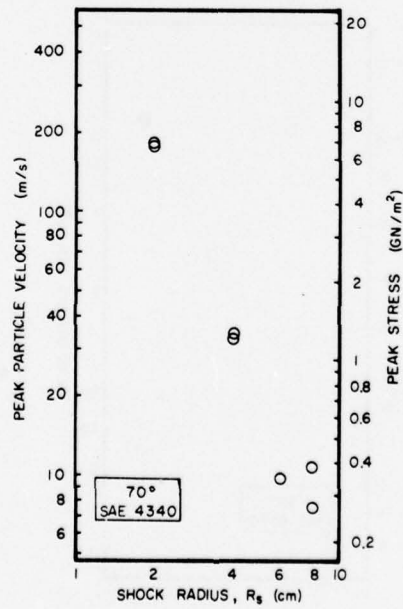Figure 38. Peak Particle Velocity Versus Radius for SAE-4340 Steel at 60°

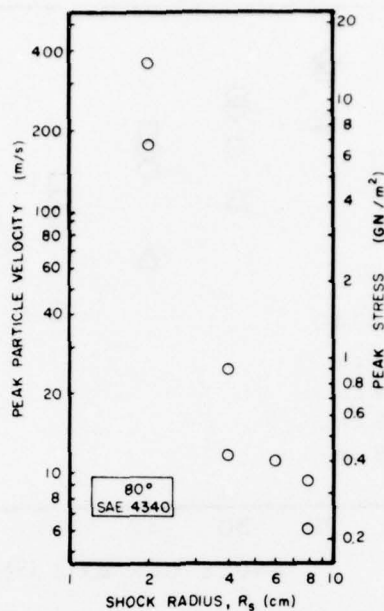Figure 39. Peak Particle Velocity Versus Radius for SAE-4340 Steel at 70°

Figure 40. Peak Particle Velocity Versus Radius for SAE-4340 Steel at 80°

radius returned data. As with the SAE 1020 steel hemispheres, the data at r = 3 cm and 2 cm are relatively uncertain, 3 cm data being the worse. There is no evidence of the bilinear behavior of $\partial \ell nu / \partial \ell nr$, as was observed in the 1020 targets. The average and standard deviation of $\partial \ell nu / \partial \ell nr$ for $\theta \leq 60°$ was 2.03 and 0.11; thus, very nearly $u \sim r^{-2}$. Beyond $\theta = 70°$ the decay was steeper.

Departure angle dependence was brought out by averaging and normalizing peak stress, as shown in Figure 41. Systematic errors in this figure may arise from errors in the normalizing stress; from Figure 32 these may be estimated at about 15 percent. Consideration of the rate of peak stress fall off with departure angle is less sensitive to this uncertainty. However, the only dependence on r evident in Figure 41 is that at r = 2 cm stress fall off with angle is less rapid. As discussed previously, this may be a consequence of the target breakup process which resulted in the observed free surface motion.

Failure modes as revealed by target cross-section were similar to those observed in the 1020 hemispheres. For example, Figures 42 and 43 show view of an 8 cm diameter target. The cracks are radial. It appears that they formed first in a region about 12 mm from the free surface.

39
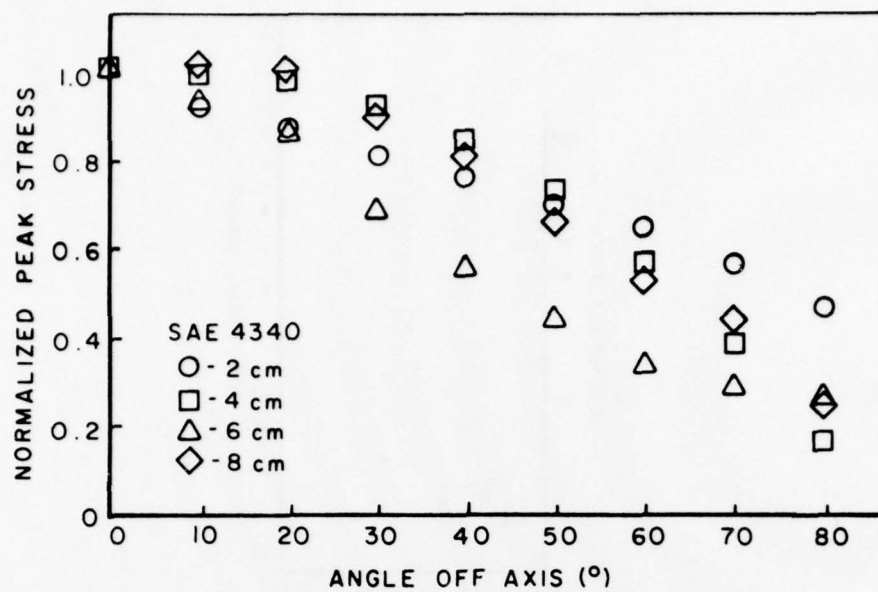
Figure 41.   Variation of Peak Shock Stress with Departure Angle
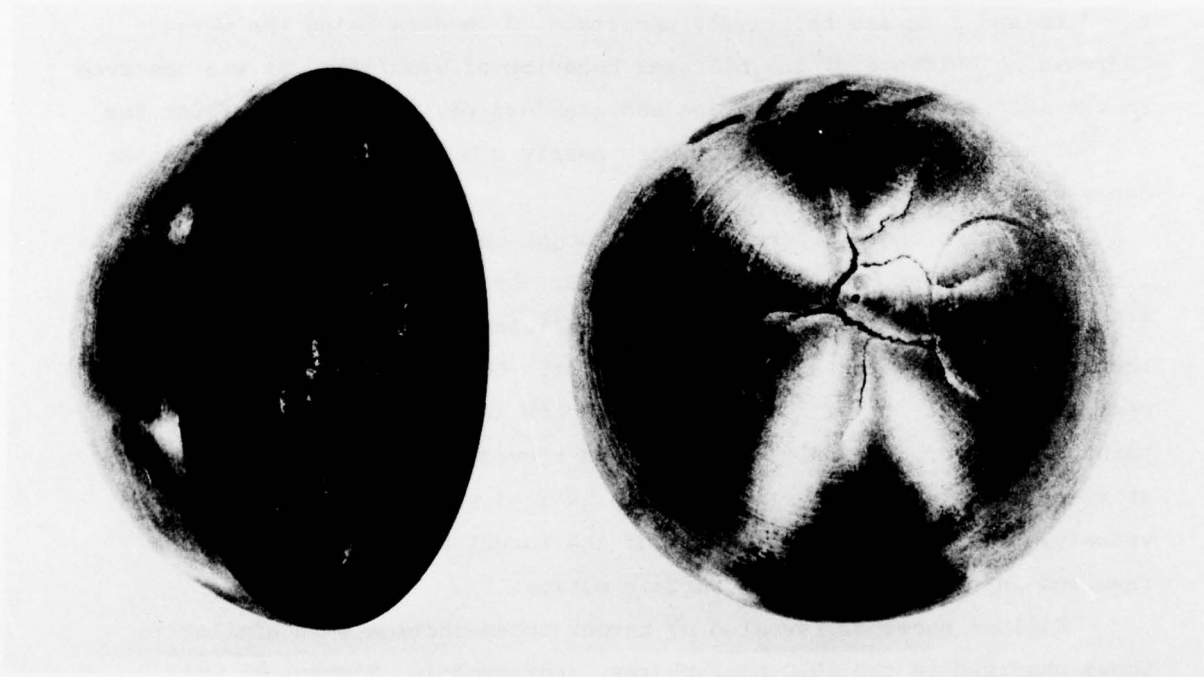
Figure 42.   Post-impact Condition of an 8 cm Diameter 4340 Target

40

Figure 43. Post-impact Cross-section of an 8 cm Diameter 4340 Target

Most crack growth occurred at small departure angles and cracks grew mostly out, not in. The cracks are jagged and the failure followed grain boundaries. Figure 44 illustrates the microstructure of this material near one of the cracks. The cracks are very shallow in the meridian plane, as were found in the 1020 targets.

Figure 44. Micrograph of Post-impact Cross-section of an 8 cm Diameter
4340 Target

SECTION V

SUMMARY

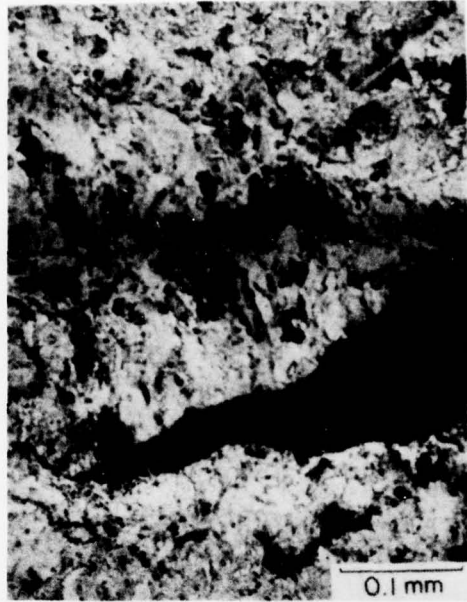The tensile strengths of 1020 and annealed 4340 steel are rate dependent. In one-dimensional stress experiments, the flow stress doubled in 1020 steel and increased 30 percent in 4340 steel between 10^{-4}/s and 10^3/s. Details are presented in Figures 12 and 13.

Dynamic failure in steel targets struck by 3 km/s projectiles was primarily a function of target geometry. Hemispherical targets of scaled radius (target radius/projectile diameter) 3.6 or less completely fragmented. Targets of scaled radius 5.4 were perforated, but otherwise intact. Failure of the 7.2 scaled radius targets was incipient. The hemispherical targets failed in biaxial tension. Cylindrical targets of the same thickness failed in spall; the spall plane was parallel to the impact surface. No differences in failure due to target composition were observed. The difference in failure mode between the hemispherical and cylindrical targets was qualitatively explained by release wave structure, as shown in Figure 31.

Peak particle velocity decay with radius and departure angle was measured. The observations could be expressed as $u \sim r^{-2}$. Decay of peak particle velocity with departure angle was similar in both materials.

A much more complete discussion of the physical processes which occurred in these experiments must await the conclusion of finite difference calcalculations, which are being conducted separately at the Air Force Armament Technology Laboratory.

REFERENCES

1. J. O. Erkman, "Smooth Spalls and Polymorphine in Iron", J. Appl. Phys. 32, 939-949, 1961.

2. L. V. Al'tshuler, S. A. Novikov, and I. J. Divnov, "The Relationship Between the Critical Breaking Stresses and the Time of Failure as a Result of the Explosive Stressing of Metals", Sov. Phys-Doklody 11, 79-82, 1966.

3. A. G. Iranov, S. A. Novikov, and Yu I. Tarasov, "Fragmentation Phenomena in Iron and Steel Caused by Explosive Shock Wave Interactions", Sov. Phys-Solid State, 4, 177-185, 1962.

4. S. A. Novikov, I. I. Divnov, and A. G. Ivanov, "Failure of Steel, Aluminum and Copper Under Extreme Shock Loading", Fiv. Metalloved. 21, 607-615, 1966.

5. F. R. Tuler and B. M. Butcher, "A Criterion for the Time Dependence of Dynamic Fracture", Int. J. Fracture Mech. 4, 431-437, 1968.

6. T. W. Barbee, L. Seaman, R. Crewdson, and D. Curran, "Dynamic Fracture Criteria for Ductile and Brittle Metals", J. Mat'ls, JMLSA, Vol. 7, 393-401, 1972.

7. J. P. Wright and L. Whitman, "Tensile Behavior of Geological Material in Ground Shock Calculations, II, DNA 4450T, March 1977.

8. J. Mescall and R. Papirno, "Spallation in Cylinder-Plate Impact", Exp. Mech., 257-266, July 1974.

9. F. E. Walker and R. J. Wasley, "Critical Energy for Shock Initiation of Heterogeneous Explosives", Explosivstoff 17, 9-13, 1969.

10. Y. de Longueville, "Description D'une mode opératoire standard pour l'etude de la sensibilité des explosifs condenses a l'onde de choc. Application uhe composition coulé". Rapport 19/74, I.S.L. (NTIS #N75-31277) 1975.

11. T. W. Barber, L. Seaman, and R. C. Crewdoor, "Dynamic Fracture Criteria of Homogeneous Materials", AFWL-TR-70-99, November 1970.

12. L. Seaman and D. A. Shockey, "Models for Ductile and Brittle Fracture Criteria for Homogeneous Materials", AFWL-TR-71-156, December 1971.

13. D. A. Shockey, L. Seaman, D. R. Curran, P. S. DeCarli, M. Austin, and J. O. Wilhelm, "A Computational Model for Fragmentation of Armor Under Ballistic Impact", AD004672, 1973.

14. J. W. Taylor, "Experimental Methods in Shock Wave Physics", in Metallurgical Effects at High Strain Rates, AIME, pp 102-128, 1973.

15. R. F. Prater, "Hypervelocity Impact - Material Strength Effects on Crater Formation and Shock Propagation in Three Aluminum Alloys", AFML-TR-70-295, December 1970.

16. for example, L. M. Barker and R. E. Hollenbach, "Shock-Wave Study of the $\alpha \rightarrow \epsilon$ Phase Transition in Iron, J. Appl. Phys. 45, 4872-4887, 1974.

17. T. Nicholas and M. J. Sever, "Dynamic Compressive Strain Rate Tests on Several Grades of Beryllium", AFML-TR-74-224, November 1974.

18. "Aerospace Structural Metals Handbook", AFML-TR-63-115, 1975 Publication.

19. U. S. Lindholm and R. L. Bessey, "A Survey of Rate Dependent Strength Properties of Metals", AFML-TR-69-119, April 1969.

20. B. M. Butcher and J. R. Canon, "Influence of Work-Hardening on the Dynamic Stress-Strain Curves of 4340 Steel", AIAA Journ., 2174-2179, December 1969.

21. M. Guinan and D. N. Beshers, "Pressure Derivatives of the Elastic Constants of Iron to 10 kbars", J. Phys. Chem. Solids 29, 541-549, 1968.

22. C. L. Mader, "An Equation of State for Iron Assuming an Instantaneous Phase Change", LA-3599, TID-4500, December 1966.